Hybrid Bilayered Vanadium Oxide Electrodes with Large and Tunable Interlayer Distances in Lithium-Ion Batteries

Xinle Zhang [†], Ryan Andris [†], Timofey Averianov [†], Michael J. Zachman [‡], Ekaterina Pomerantseva [†*]

† *Department of Materials Science and Engineering, Drexel University, Philadelphia, PA 19104, USA*

‡ *Center for Nanophase Materials Sciences (CNMS), Oak Ridge National Laboratory, Oak Ridge, TN 37830, USA*

* *Corresponding Author:* ep423@drexel.edu

Keywords: layered oxide; tunable interlayer distance; hybrid materials; chemical preintercalation; cathodes; lithium-ion batteries

Abstract: The interlayer distances in layered electrode materials, influenced by the chemical composition of the confined interlayer regions, have a significant impact on their electrochemical performance. Chemical preintercalation of inorganic metal ions affects the interlayer spacing, yet expansion is limited by the hydrated ion radii. Herein, we demonstrate that using varying concentrations of decyltrimethylammonium (DTA^+) and cetyltrimethylammonium (CTA^+) cations in chemical preintercalation synthesis followed by hydrothermal treatment, the interlayer distance of hybrid bilayered vanadium oxides (BVOs) can be tuned between 11.1 Å and 35.6 Å. Our analyses reveal that these variations in interlayer spacing are due to different amounts of structural water and alkylammonium cations confined withing the interlayer regions. Increased concentrations of alkylammonium cations not only expand the interlayer spacing but also induce local bending and disordering of the V-O bilayers. Electrochemical cycling of hybrid BVO electrodes in non-aqueous lithium-ion cells show that specific capacities decrease as interlayer regions expand, suggesting that the densely packed alkylammonium cations obstruct intercalation sites and hinder Li^+ ion transport. Furthermore, we found that greater layer separation facilitates the dissolution of active material into the electrolyte, resulting in rapid capacity decay during extended cycling. This study emphasizes that layered electrode materials require both spacious interlayer regions as well as high structural and chemical stabilities, providing guidelines for structural engineering of organic-inorganic hybrids.

Graphical Abstract

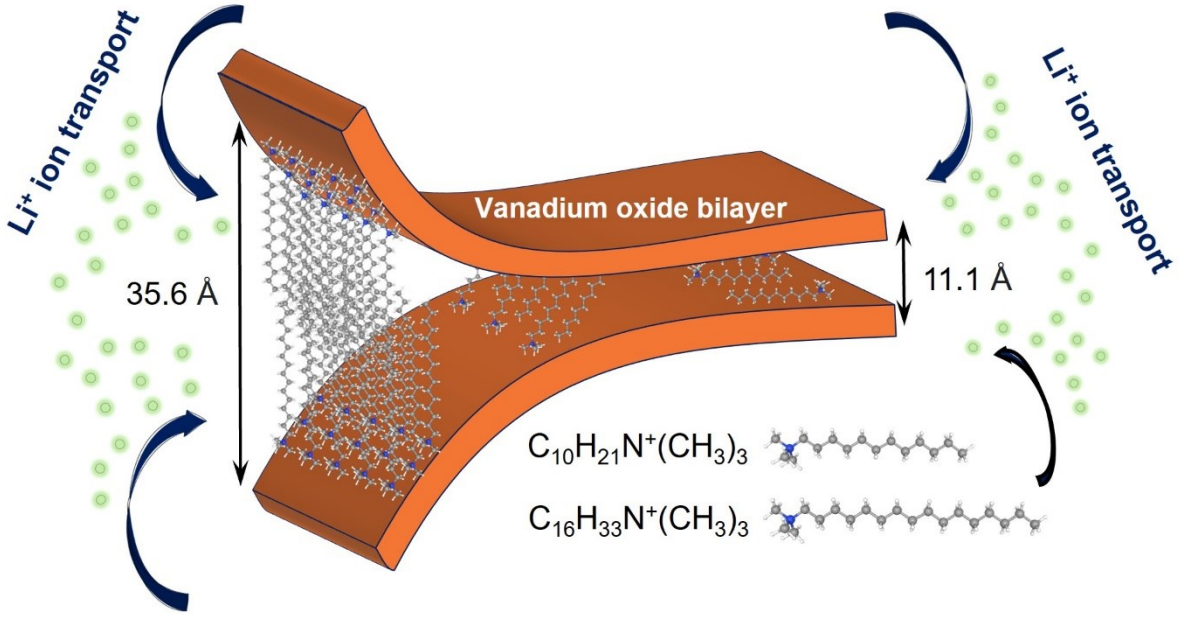

(abstract figure)

Introduction

Intercalation-type batteries open pathways for transitioning to energy-sustainable solutions, such as the electrification of transport and the storage of clean energy. Lithium-ion batteries (LIBs) stand as the most advanced and efficient battery systems, releasing energy due to the intercalation of Li^+ ions into the crystal structure of the cathode material. Transition metal oxides based on vanadium [1-3], manganese [4-7], and nickel [8-10] have shown promise in Li^+ ion storage properties; theories and characterization methodologies have been established to understand their structural features [11], phase transformations and failure mechanisms [4-6]. Layered transition metal oxides (LTMOs) that feature open two-dimensional (2D) ion transport channels have received considerable attention as cathode materials [12-16]. It has been proposed that expanding the interlayer distance of layered electrode materials can weaken the Faradaic interactions between electrolyte ions and electrode materials [17], facilitating the diffusion of charge-carrying ions (Li^+ ions in case of LIBs), thus leading to improved cyclability and power density [18]. For instance, a general methodology demonstrated that using alkali metal ions to expand the interlayer regions of layered vanadium and molybdenum oxides enhanced their electrochemical stability and rate capability in Li-ion cells due to the increased diffusion of Li^+ ions [19]. Another study showed that the confinement of alkyldiamines in layered MoS_2 led to the expansion of the interlayer region and reduced crystal size, which increased pseudocapacitive behavior and Li^+ ion storage capacity [20]. Bilayered vanadium oxide (BVO or δ-$V_2O_5{\cdot}nH_2O$) is a promising intercalation cathode candidate due to its relatively high redox potential, theoretical capacity and large interlayer distance of 11.5 Å. [21-24]. The interlayer distance of BVO is more than twice that of commonly employed layered cathode materials for LiBs, such as nickel cobalt manganese oxide and nickel cobalt aluminum oxide (4.7-4.8 Å) [25, 26], thus enabling a high initial capacity for Li^+ ion storage [27]. However, the pristine BVO phase exhibits structural stability issues, resulting in rapid capacity decay over extended electrochemical cycling [21, 22]. Chemical preintercalation is a versatile synthesis strategy that has been demonstrated to improve the cycling performance of BVO by inserting water-soluble species into its crystal structure prior to electrochemical cycling [28]. The chemical preintercalation synthesis approach was initially developed by inserting Na^+ ions into the interlayer region of BVO which was shown to facilitate the diffusion of Na^+ ions in Na-ion batteries [29]. Subsequently, the versatility of the chemical preintercalation synthesis has been demonstrated by five BVOs chemically preintercalated with alkali and alkali-earth metal ions (δ-$M_xV_2O_5{\cdot}nH_2O$, where M stands for Li, Na, K, Mg, or Ca) that showed improved electrochemical cycling performance in Li-ion cells [30, 31]. δ-$Mg_xV_2O_5{\cdot}nH_2O$ (MVO) delivered the highest specific capacity and cycling stability, attributed to its most expanded interlayer distance of 13.4 Å compared to the other four phases [30]. Therefore, it is believed that further expansion of the interlayer distance beyond that achieved in the MVO phase might potentially improve the electrochemical performance of the chemically preintercalated BVOs.

The tunability of structures and electronic properties of multiple transition metal oxides has been demonstrated by forming organic-inorganic hybrid structures through templating with various organic molecules [32, 33]. When it comes to adjusting the interlayer distance of LTMO electrodes, chemical preintercalation synthesis using large and water-soluble templating organic molecules could be a more effective strategy than using small inorganic metal ions. Additionally, the chemical preintercalation synthesis requires the organic compounds to be positively charged so they can be trapped within the negatively charged interlayer regions. Linear organic cations are a family of water-soluble organic compounds, forming due to the dissociation of corresponding salts, that possess both hydrocarbon alkyl chain and positively charged hydrophilic head in their linearly shaped molecular structure. The linear organic cations such as primary amine or alkylammonium are larger than inorganic ions and can self-assemble on or within negatively charged surfaces, thus serving as ideal candidates to form hybrid layered oxides. Previous work has shown the synthesis of hybrid BVO electrode materials enabled by chemically preintercalating three types of positively-charged alkylammonium ions, demonstrating that a high concentration of organic cations during the chemical preintercalation synthesis is necessary to expand the interlayer region substantially, up to 30.5 Å [34]. These hybrid electrodes with expanded interlayer region exhibited improved electrochemical cycling stability in both Li-ion and Na-ion cells [34]. Similar organic cations have also served as liquid templates in the synthesis of nanostructured electrode materials [35, 36]. Vanadium oxide nanotubes (VO_x-NTs) with open-end and muti-wall structures were synthesized via hydrothermal treatment using primary alkylamines acting as the structure-directing agents [37-39]. These structure-directing molecules introduced nanometer-scale (2-4 nm) cavities in the multi-wall structure, which is designated to facilitate the ion-exchange procedure without significantly changing the structure of nanotubes [38, 40]. Another study revealed how the length and concentration of the confined alkylammonium cations within the interlayer regions of $Ti_3C_2T_x$ MXene impact its *d*-spacing and electrochemical properties [41]. Recent studies also reported the formation of hybrid vanadium oxides via chemical preintercalation of organic species such as ferrocenium [42], methylthioninium [43], naphthoquinone [44], or benzoquinone [45], which led to the expansion of the interlayer distances up to 19.05 Å, thus creating fast channels for rapid diffusion of the electrochemically cycled ions. Nevertheless, varying the concentrations of chemically preintercalated organic species in the interlayer regions of BVO and their correlation to interlayer distances and charge storage properties have rarely been investigated.

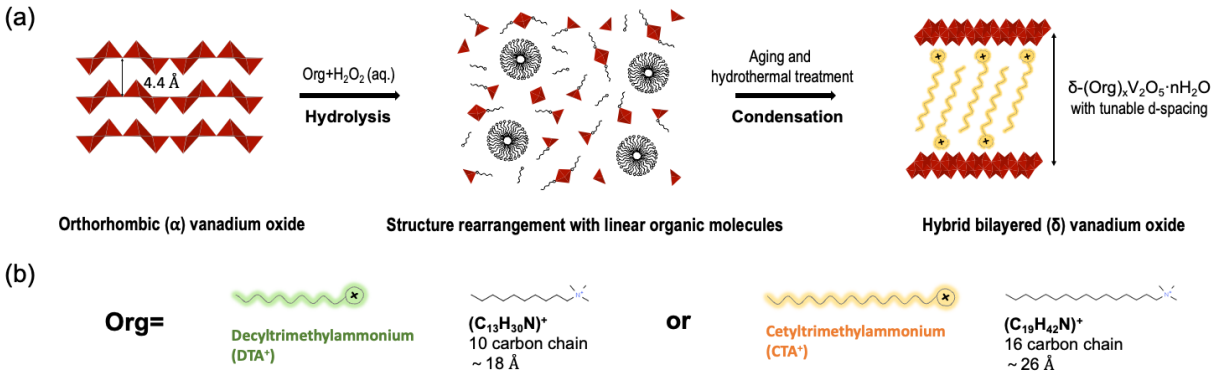

Figure 1. (a) Schematic illustration of chemical preintercalation synthesis and post-synthesis treatments of $(DTA)_xV_2O_5$ and $(CTA)_xV_2O_5$ phases that exhibit organic-inorganic hybrid structures; (b) Structure illustrations and chemical formula of the decyltrimethylammonium (DTA^+) and cetyltrimethylammonium (CTA^+) cations.

In this work, we demonstrate that by varying the length and concentration of the alkylammonium cations in chemical preintercalation synthesis **(Figure 1)**, the interlayer distances of $(Org)_xV_2O_5{\cdot}nH_2O$ (hybrid BVOs) can be varied from 11.1 Å to 35.6 Å. We also demonstrate that hydrothermal treatment of the aged hybrid BVOs not only improves the phase crystallinity as previously observed [29], but also induces interlayer distances to further change. The average interlayer distances of the hybrid BVOs were determined by calculating *d*-spacings from (001) reflections in X-ray diffraction (XRD) patterns. These generally agreed with measurements by scanning transmission electron microscopy (STEM), which additionally revealed local disorder in the BVO layers and interlayer distances. These observations suggest that confined cations could be unevenly distributed in the interlayer regions. Thermogravimetric analysis (TGA) curves of hybrid BVOs were acquired to compare the differences in concentration of the confined cations for the synthesized hybrid BVO phases. Fourier transform infrared spectroscopy (FTIR) spectra of the hybrid BVOs with different confined cations concentrations were acquired to understand the competing mechanism between the structural water and the amphiphilic cations during the chemical preintercalation synthesis. The electrochemical properties and cycling performance of the hybrid BVOs with various interlayer distances were evaluated in non-aqueous Li-ion cells, revealing that the specific capacity, cycling stability, and rate capability of hybrid BVOs improve with the decrease in the interlayer spacing. Our results shed light on the considerations for hybrid electrode material design as well as the possible degradation mechanisms of the layered hybrid electrodes with the interlayer regions expanded to a few nanometers.

Experimental Methods

Synthesis of hybrid BVOs

Hybrid BVOs were synthesized using the chemical preintercalation method [28] with some of the parameters adjusted [46] to ensure the incorporation of linear organic cations as specified below. 0.5 g of commercially available V_2O_5 powder (99.6%, Alfa Aesar) were mixed with decyltrimethylammonium bromide (99.0%, DTAB, Acros Organics) or cetyltrimethylammonium bromide (100.0 %, CTAB, MP Biomedicals) in 15 mL deionized water under vigorous stirring. Organic-bromide salts (DTAB or CTAB) to vanadium oxide molar ratios (Org:V_2O_5) of 1:1, 1:2, 1:5, 1:10, 1:20 were used. To initiate the hydrolysis reaction, 8 ml of 30 vol% hydrogen peroxide (H_2O_2, Fisher Scientific) were added dropwise to the suspension over 2 h while stirring vigorously. During the first hour of H_2O_2 addition, the mixture was kept at a room temperature; then the temperature was increased to 60ºC. After 8 mL of H_2O_2 were added, the mixture was kept under stirring at 60℃ for 4 h to allow the formation of the chemically preintercalated precipitates. The precipitates were covered by Parafilm in beakers and aged at room temperature for 4 days [29]. The aged precipitates were washed and filtered with a copious amount of deionized water to ensure the removal of the residual bromide salts and unprecipitated vanadium species. For each sample, half of the aged precursor was directly dried at 105°C in air. The remaining aged precursors were transferred to 23 mL Teflon-lined stainless-steel autoclaves and hydrothermally treated with 15 mL of deionized water at 160 °C for 24 h. The hydrothermally treated products were also washed with copious amounts of deionized water and dried at 105°C in air. For the ease of discussion, the hydrothermally treated hybrid BVOs with 1:2, 1:5, and 1:20 Org:V_2O_5 ratio were denoted as DTAVO2, DTAVO5, DTAVO20 and CTAVO2, CTAVO5, CTAVO20, respectively.

Physical Characterizations

Powder X-ray diffraction (XRD) analysis was carried out using Rigaku MiniFlex 600 diffractometer equipped with Cu-Kα radiation (λ = 1.54 Å). The diffraction patterns were acquired from 2 to 55° 2θ with a step size of 0.02° 2θ and a step duration of 1 s. Backgrounds in XRD data were subtracted using *CrystalDiffract 6* software to remove the non-crystallographic information. The *d*-spacings were calculated from the positions of (001) reflections using *Bragg's law*. The SEM images were captured using a Zeiss Supra 50VP (Zeiss, Germany) scanning electron microscope equipped with Schottky field emission and Everhart–Thornley in-lens secondary electron detectors. The electron beam accelerating voltage of 5kV was applied. All samples were sputter-coated with a thin layer of Pt/Pd to avoid image drifting. FTIR sample discs were prepared by mixing 1 mg of the active material with 200 mg of KBr powder (ACS reagent, ≥ 99.0%) and pressing them in a 13 mm pellet mold at 50 psi. FTIR spectra in transmission mode were

recorded using an INVENIO FT-IR Spectrometer (Bruker, U.S.A.) between 400 and 4000 cm^{-1}. XPS measurements were recorded on a Physical Electronics VersaProbe 5000 instrument using a monochromatic Al Kα source and ionized Ar for charge compensation. The high-resolution V *2p* spectra were taken at a pass energy of 23.5 eV with a step size of 0.05 eV. Peak fitting and data analysis were carried out using *CasaXPS* software. A Shirley background was used for V *2p* spectra quantification. Thermogravimetric analysis (TGA) curves were obtained using a Q50 analyzer (TA Instruments, USA) in air between 25°C - 1000°C with a temperature ramp of 10°C min^{-1}. High-resolution aberration-corrected STEM imaging was performed on a JEOL NEOARM (JEOL USA, Peabody, MA), which was operated with an accelerating voltage of 200 kV and a convergence angle of ~28 mrad. STEM samples were produced by dispersing specimen powders in acetone, sonicating, and drop casting onto a copper TEM grid coated with lacey carbon. Samples were stored in a desiccator prior to preparation and rapidly transferred to the bake cart/instrument vacuum after preparation. The dissolution of the hybrid BVOs for atomic absorption spectroscopy (AAS) measurements was simulated by mixing 15 mg (±0.3 mg) of hybrid BVO powder with 10 mL (±0.2 mL) of electrolyte solvent (EC/DMC = 50/50 vol%) and letting them interact for two days. Then, AAS samples were prepared by taking 1.5 mL of the supernatant and diluting to 25 mL in water using 3 vol% H_2O_2 (aq.) solution to prevent precipitation. A vanadium calibration curve was developed using 5, 10, 15, and 20 µg/mL vanadium standard solutions that were diluted from a 1000 µg/mL standard solution (Inorganic Ventures, USA) with analytical grade water. The vanadium concentration in each sample was determined using an AA-7000 flame atomic absorption spectrometer (Shimadzu, Japan) with a C_2H_2-N_2O flame. A flame optimization setup was performed, and the vanadium lamp was warmed up for 5 minutes before performing the AAS analysis.

Electrochemical Characterizations

Electrode slurries were prepared by mixing 70 wt% active material, 20 wt% carbon black, and 10 wt% PVDF (polyvinylidene fluoride, Arkema) in NMP (99.5% 1-Methyl-2-pyrrolidinone, Acros Organics) using a Flacktek SpeedMixer. The active material and carbon black were manually ground in a mortar with pestle prior to mixing with PVDF solution in NMP. The slurries were cast onto aluminum foil using a doctor blade to achieve a uniform thickness of 80 µm. The electrode films were dried at 105°C under vacuum overnight. Subsequently, 10 mm electrode disks were punched from the electrode films and dried at 105°C under vacuum overnight before being transferred to an argon-filled glove box. All electrochemical data were obtained using type 2032 coin cells with a two-electrode configuration. Lithium metal disks (99.9%, 12 mm × 0.75 mm, AOT battery) served as both counter and reference electrodes. 1M lithium perchlorate ($LiClO_4$, 99.99%, Sigma-Aldrich) dissolved in ethylene carbonate (EC, Gotion Inc.) / dimethyl carbonate (99.99%, DMC, Acros Organics) (50/50 vol%) served as electrolyte and monolayer

polypropylene membrane (Celgard 3501, USA) served as separator. All materials were tested in a voltage window of 2.0-4.0 V versus the Li/Li^+ reference. Cyclic voltammetry (CV) curves were obtained using a VMP3 potentiostat (Biologic, USA) with a scan rate of 0.1 mV s^{-1}. Galvanostatic cycling experiments were performed using an Arbin electrochemical workstation (Arbin Instruments, USA) under a current density of 20 mA g^{-1}, and the rate capability was assessed by cycling for 10 cycles at each of the following current densities: 20, 50, 100, 200, and 20 mA g^{-1}, respectively. All cells were assembled in an argon-filled glovebox and allowed to rest for 1 hour before being cycled at room temperature. The potentials are reported with respect to the Li/Li^+ reference electrode throughout the manuscript.

Results and Discussion

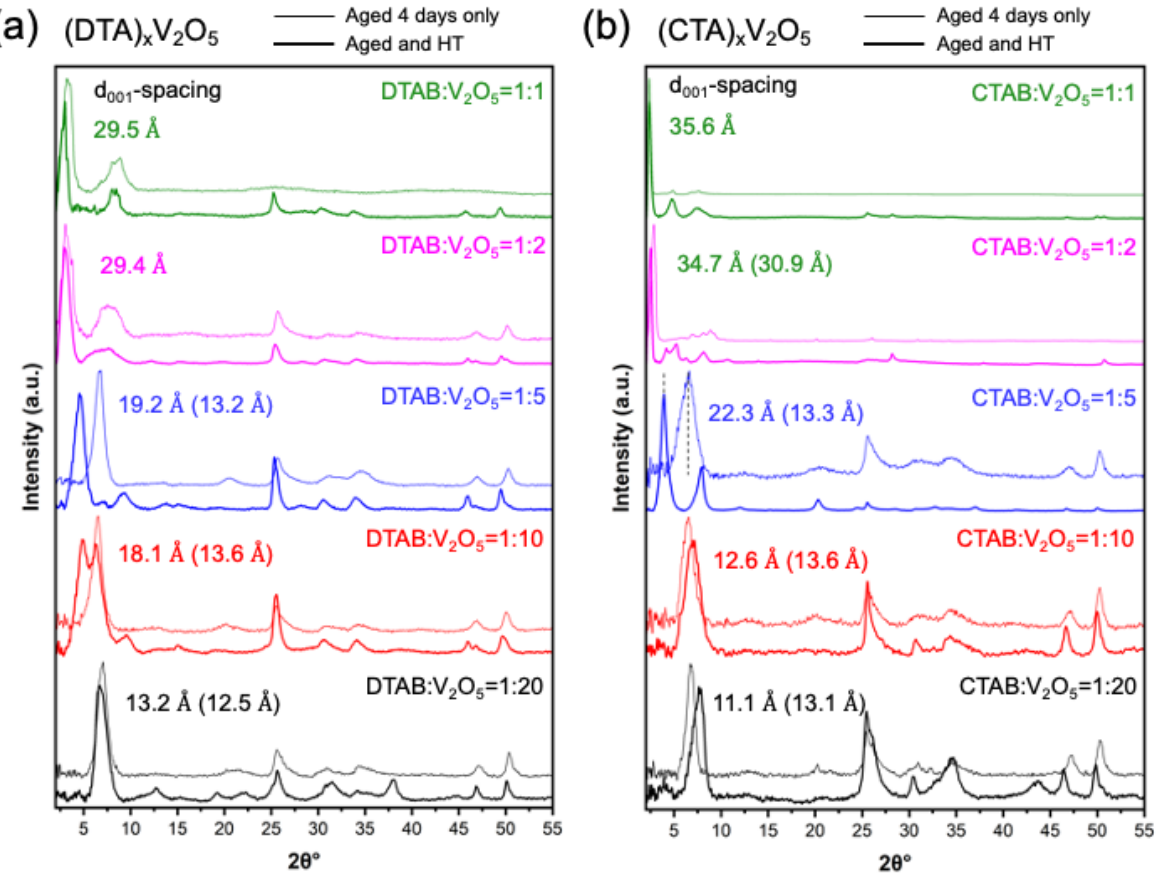

Figure 2. XRD patterns of (a) $(DTA)_xV_2O_5$ and (b) $(CTA)_xV_2O_5$ synthesized using different Org:V_2O_5 molar ratios before (thin lines) and after (thick lines) hydrothermal treatment (HT). Corresponding Org:V_2O_5 ratios are labeled in the figure. The *d*-spacings are shown next to the (001) reflection, where the number shown without parentheses corresponds to the sample obtained after HT, and the number shown in parentheses corresponds to the aged only sample.

The XRD patterns of the DTA^+ and CTA^+ preintercalated hybrid BVOs (referred to as $(DTA)_xV_2O_5$ and $(CTA)_xV_2O_5$, respectively) synthesized using the Org:V_2O_5 ratio ranging from 1:20 to 1:1 before and after hydrothermal treatment (HT) are shown in **Figure 2**. For aged $(DTA)_xV_2O_5$ and $(CTA)_xV_2O_5$ before HT, the (001) diffraction peak shifts to a lower 2θ angle as the Org:V_2O_5 ratio increases, indicating a *d*-spacing increase. For the lower Org:V_2O_5 ratios (1:5, 1:10 and 1:20), the *d*-spacings are consistent and all below 14 Å regardless of the length of the chemically preintercalated linear organic cations. When Org:V_2O_5 ratio increased to 1:2, the *d*-spacing of aged $(DTA)_xV_2O_5$ and $(CTA)_xV_2O_5$ increased to 29.4 Å and 30.8 Å, respectively. This observation suggests that the orientation of the confined DTA^+ or CTA^+ cations in phases synthesized with higher Org:V_2O_5 ratios might be different from the phases synthesized with lower Org:V_2O_5 ratios. Since the DTA^+ or CTA^+ cations are primarily linear alkyl chains tens of angstroms long and a few angstroms wide, the orientation of DTA^+ or CTA^+ cations could be parallel to the V-O bilayers in the lower Org:V_2O_5 ratio phases, and gradually tilted up when the Org:V_2O_5 ratio increases. Such a change in the orientation of the confined cations could inevitably lead to the expansion of the interlayer regions (**Figure S1** in **Supporting Information**). Stable *d*-spacings of $(DTA)_xV_2O_5$ (29.4 – 29.5 Å) and $(CTA)_xV_2O_5$ (34.7 – 35.6 Å) synthesized using Org:V_2O_5 ratio of 1:2 and 1:1, respectively (**Figure 2**), suggest that Org:V_2O_5 ratio of 1:2 for chemical preintercalation synthesis is sufficient for a more vertically aligned orientation of the confined DTA^+ or CTA^+ cations. The XRD patterns of the hydrothermally treated $(DTA)_xV_2O_5$ and $(CTA)_xV_2O_5$ showed the shifted and narrowed reflection peaks, indicating the HT caused the crystallinity improvement and further *d*-spacing change. The *d*-spacing of the DTAVO5 increased from 13.2 Å to 19.2 Å (~6 Å) and CTAVO5 increased from 13.3 Å to 22.3 Å (~9 Å) due to HT. Interestingly, the XRD pattern of DTAVO10 shows a splitting of (001) peak with *d*-spacings of 13.6 Å and 18.1 Å, respectively. This observation indicates the possibility of the formation of two hybrid BVO phases with the confined DTA^+ cations adopting two different orientations in the interlayer regions. The *d*-spacing of CTAVO20 decreased from 13.1 Å to 11.1 Å (~2 Å) after HT, which could indicate re-arrangement of the initial positions of the hydrophobic tails of CTA^+ cations, accompanied by the partial removal of interlayer water molecules.

The DTAVO2, DTAVO5, DTAVO20, CTAVO2, CTAVO5 and CTAVO20 samples were selected for more extensive characterizations. The morphology of these materials is shown in **Figure S2** and **Figure S3** (**Supporting Information**). Since the broad XRD peaks indicate that the hybrid phases are composed of layered crystal structures with short-range periodicity, the interlayer distances measured from the bulk phase might show deviation from its local structure. Therefore, scanning transmission electron microscopy (STEM) was performed to verify the local geometry and interlayer spacings of each sample. High-angle annular dark-field (HAADF) STEM images of six selected phases are shown in **Figure 4**. DTAVO20 is composed of vanadium oxide bilayers with an average measured spacing of ~9.1 Å, which is larger than

previously observed bilayer phases[46]. Interestingly, DTAVO5 and DTAVO2 are composed of V-O bilayers with alternating interlayer spacings that are smaller and larger than those in DTAVO20. This results in pairs of closely spaced V-O bilayers, or "quad-layers," separated by larger spacings (**Figure 3b,c**). The spacings between these quad-layers range from 18.1 to 20.7 Å for DTAVO5 and 20.8 Å to 36.3 Å for DTAVO2 in these images. Although none of the CTA^+ preintercalated phases have alternating spacing like the DTA^+ preintercalated phases, a range of interlayer distances is present that is broader for higher linear organic molecule concentrations. The average interlayer spacing for CTAVO20 is ~10.1 Å, an ~1 Å deviation compared to the XRD measurement, which could be attributed to the varying spacings present combined with local nature of STEM measurements[47]. In addition, the local CTAVO5 interlayer spacings shown in **Figure 3e** range from 17.3 to 23.3 Å and the individual bilayers resultingly have local curvature variations to accommodate these spacings (**Figure S1**). These interlayer spacings and layer curvature inhomogeneities at higher linear organic molecule concentrations may be due to unevenly packed CTA^+ molecules and have not been observed in BVOs chemically preintercalated with inorganic ions. We only observed up to ~23 Å in the CTAVO2 ratio sample by STEM, compared to ~36 Å measured by XRD, which may indicate different interlayer spacings are present at the edges compared to the interiors of particles, since STEM is conducted on thin, near-surface structures, while XRD largely probes particle interiors.

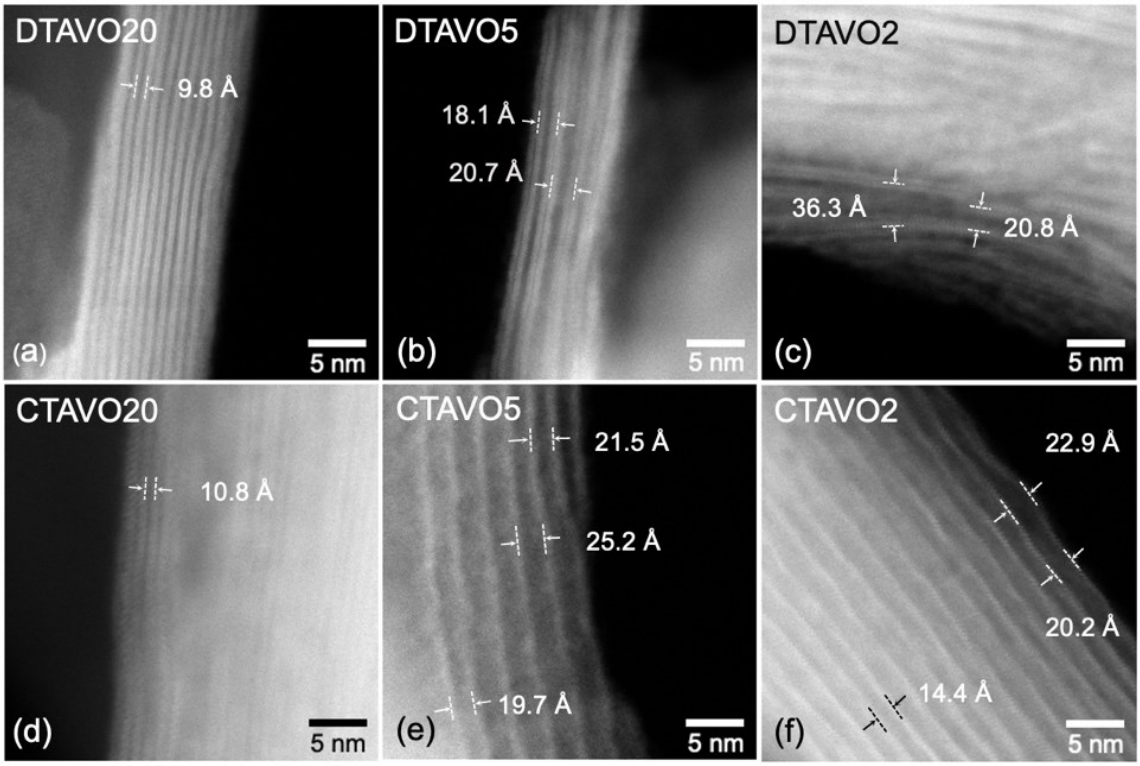

Figure 3. Interlayer distance measurements by high-angle annular dark-field (HAADF) STEM for (a-c) $(DTA)_xV_2O_5$ and (d-f) $(CTA)_xV_2O_5$ with (a, d) 1:20, (b, e) 1:5, and (c, f) 1:2 Org:V_2O_5 ratios, respectively.

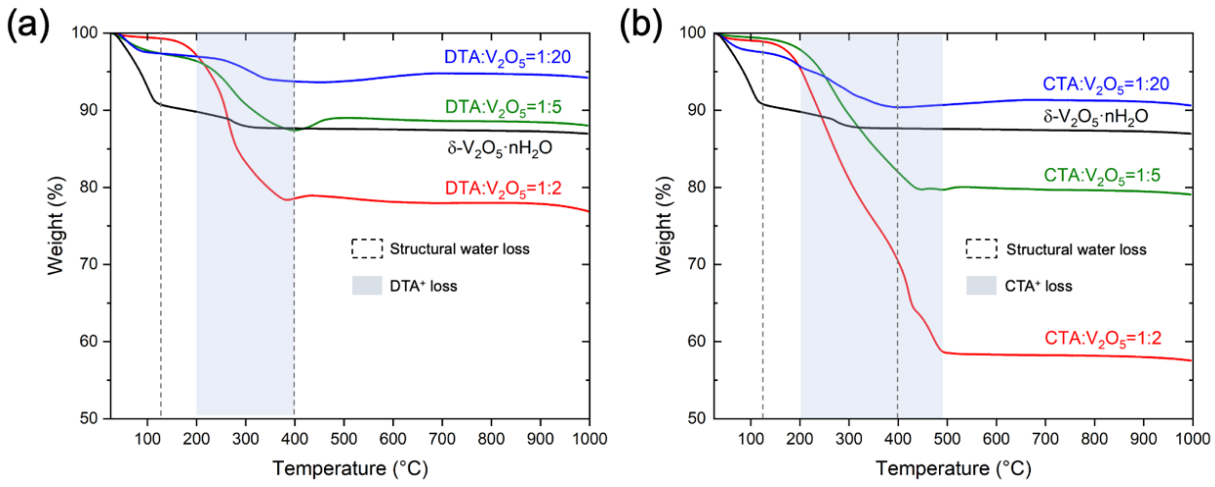

Figure 4. TGA weight loss curves of (a) $(DTA)_xV_2O_5$ and (b) $(CTA)_xV_2O_5$ synthesized using Org:V_2O_5 = 1:20, 1:5, and 1:2. Data for the pristine phase (δ-$V_2O_5 \cdot nH_2O$) with only water molecules in the interlayer region is shown for reference. The regions indicated with the dash lines correspond to the mass decrease due to the loss of structural water; the regions colored with the light blue correspond to the mass decrease due to the loss of chemically preintercalated organic cations.

TGA weight loss curves of DTAVO2, DTAVO5, DTAVO20, CTAVO2, CTAVO5 and CTAVO20 are shown in **Figure 4.** Comparing the weight loss curves of hybrid BVOs with the δ-$V_2O_5 \cdot nH_2O$ reference phase synthesized without the addition of linear organic cations reveals an overlap in the weight loss caused by removal of confined linear organic cations and structural water between 120-400 ºC. The weight loss below 120°C can be assigned to the removal of the physiosorbed water. Above 120°C, crystallographic water leaves the structure until the interlayer region is fully dehydrated at 400°C [48]. **Figure S4 (Supporting Information)** suggests that the breakdown temperature of the DTAB and CTAB salts ranges between 200 and 500°C. Because the loss of structural water and confined linear organic cations in the hybrid BVOs occurred within an extensively overlapped temperature range, the determination of the chemical composition of the hybrid phases is challenging. However, the increasing weight loss fraction of the hybrid BVOs with a higher Org:V_2O_5 ratio suggests that higher fractions of linear organic cations could be trapped in the interlayer regions of hybrid BVO during the chemical preintercalation synthesis, leading to the substantially expanded interlayer region as observed in XRD patterns and STEM images.

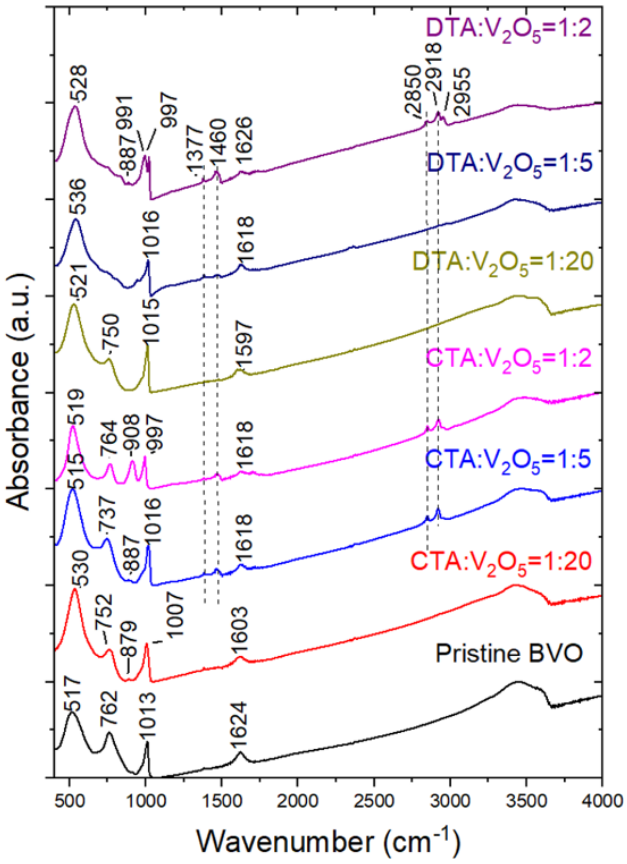

Figure 5. FTIR spectra of $(DTA)_xV_2O_5$ and $(CTA)_xV_2O_5$ synthesized using Org:V_2O_5 molar ratios of 1:20, 1:5, and 1:2. The FTIR spectrum of δ-$V_2O_5{\cdot}nH_2O$ is shown as a reference.

FTIR analysis, shown in **Figure 5**, was incorporated to further understand the chemistry of the hybrid BVOs with linear organic cations confined in their interlayer regions. The features between 400-1100 cm^{-1} correspond to the inorganic V-O fingerprint region [49, 50]. The characteristic BVO peaks include V-O-V out-of-plane stretching between 515-536 cm^{-1}, V-O-V in-plane stretching between 737-764 cm^{-1}, and V=O group stretching between 997-1016 cm^{-1}. Features from structural water appear between 1603-1626 cm^{-1} and near the ~3500 cm^{-1} region, corresponding to H-O-H bending and O-H stretching, respectively. The diminishing relative intensity of the water features as the linear organic molecule concentration increases implies that the DTA^+ and CTA^+ cations occupy the interlayer region that would otherwise possess water molecules. The reduction of water content could also be related to the hydrophobic tails from the DTA^+ and CTA^+ cations that drive the water out of the interlayer region. The FTIR features of the pure DTAB and CTAB are also observed in the spectra of the $(DTA)_xV_2O_5$ and $(CTA)_xV_2O_5$ synthesized with the Org:V_2O_5 ratios of 1:2 and 1:5. For reference, the labeled FTIR spectra of pure DTAB and CTAB salts are provided in **Figure S5** (**Supporting Information**) [51]. The peaks at ~2918 and ~2850 cm^{-1} in FTIR spectra of DTAVO2, CTAVO2 and CTAVO5 could correspond to the C-H stretching vibration from DTA^+ or CTA^+.

The peaks at 1460 and 1487 cm^{-1} could correspond to the C-N stretching vibrations from the hydrophilic heads of DTA^+ or CTA^+ cations. The features from linear organic cations exhibit relatively lower intensity compared to those corresponding to the V-O layers, suggesting the confinement effect of the interlayer regions could have suppressed the vibration features of the chemically preintercalated linear organic cations. These features follow two trends. First, the intensities scale with the concentration of confined linear organic cations, appearing most prominently in the spectra of DTAVO2 and CTAVO2 and lacking any signal in the spectra of DTAVO20 and CTAVO20. Second, the C-H stretching features are more prominent in samples preintercalated with CTA^+ rather than DTA^+, possibly due to the longer C-H chains on CTA^+ cations contributing to additional intensities.

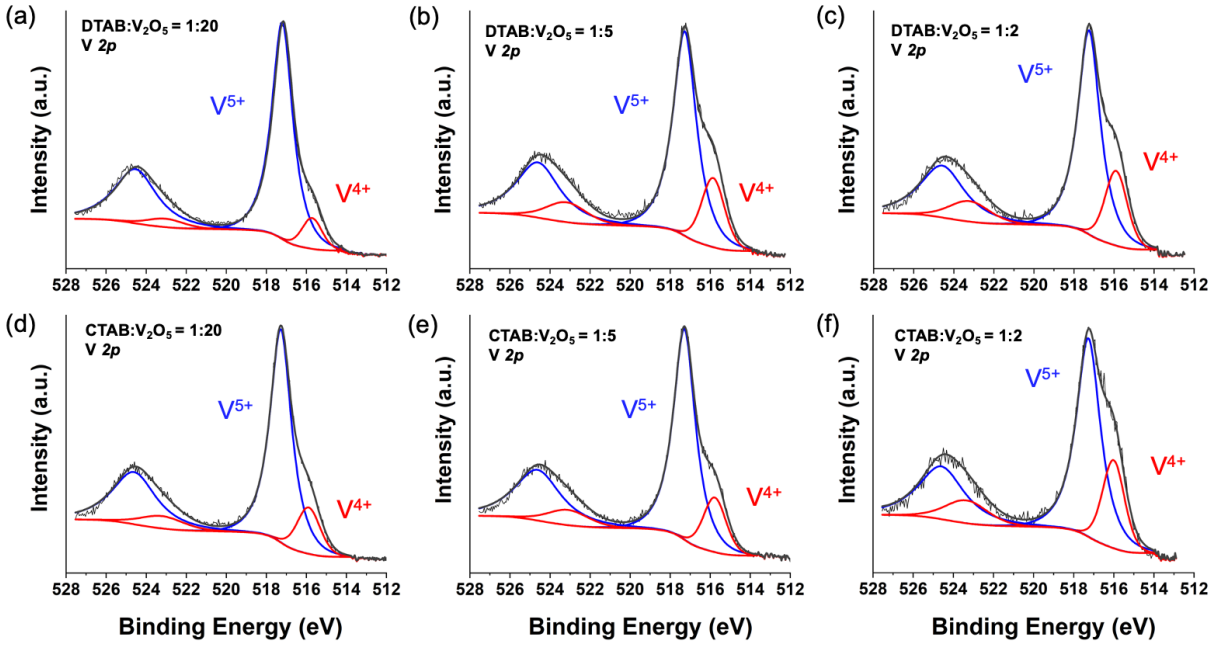

Figure 6. XPS spectra of the V2p region of (a – c) $(DTA)_xV_2O_5$ and (d – f) $(CTA)_xV_2O_5$ synthesized using Org:V_2O_5 molar ratio of (a, d) 1:20, (b, e) 1:5, and (c, f) 1:2 after HT.

XPS spectra **(Figure 6)** of six selected hybrid phases were acquired to understand how the positively charged linear organic cations impact the valence state of vanadium. The estimated V^{5+} versus V^{4+} fractions in each sample are listed in **Table 1**. The DTAVO20 spectrum shows the highest V^{5+} fraction (i.e., 90%) among the six hybrid phases, and the spectra for each respective hybrid phase show that the ratio between V^{5+} and V^{4+} generally increases as the Org:V_2O_5 ratio increases. The confined linear organic cations could reduce the vanadium according to two mechanisms. First, there could be a direct sharing of the charges between V^{5+} and the positively charged linear organic cations. Alternatively, linear organic cations with longer alkyl tails length may be stronger reducing agents. When comparing the samples synthesized with

the same Org:V_2O_5 ratio, albeit with different cations, the V^{5+} fraction in $(DTA)_xV_2O_5$ materials is generally higher than in $(CTA)_xV_2O_5$ samples. This trend could be attributed to the longer alkyl chain of the CTA^+ cations possessing more electron denoting alkyl groups than DTA^+ cations. However, the portion of V^{5+} in CTAVO5 is higher than DTAVO5. This observation could indicate that the oxidation state of vanadium in the hybrid BVOs with the same Org:V_2O_5 ratio could also depend on the interlayer distance of the sample or even the orientation of the preintercalated linear organic molecules.

Table 1 Summary table of XPS results for $(DTA)_xV_2O_5$ and (CTA)xV2O5 hybrid BVOs reporting fractions of V^{5+} and V^{4+} in each phase.

Sample #	V 2p oxidation state (at %) BE (eV)	
	V $^{5+}$ (517.2)	V $^{4+}$ (515.9)
DTAVO20	90	10
DTAVO5	78	22
DTAVO2	76	24
CTAVO20	83	17
CTAVO5	81	19
CTAVO2	74	26

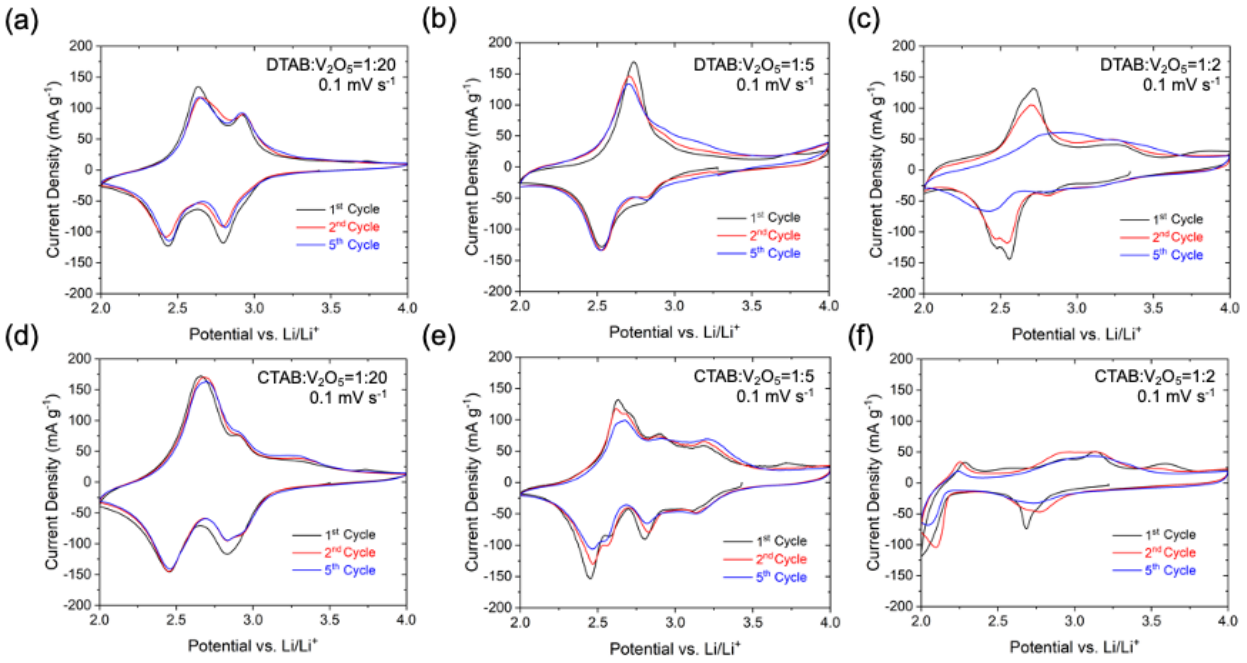

Figure 7. 1st, 2nd and 5th cycle CV curves of (a – c) $(DTA)_xV_2O_5$ and (d – f) $(CTA)_xV_2O_5$ synthesized using the Org:V_2O_5 molar ratio of (a, d) 1:20, (b, e) 1:5 and (c, f) 1:2 in lithium-ion cells with the scan rate of 0.1 mV s^{-1}.

The electrochemical cycling in non-aqueous lithium-ion cells was performed to evaluate the electrochemical charge storage properties of the selected hybrid BVOs across a wide range of interlayer distances (**Figure 7**). DTAVO20 and CTAVO20 exhibited two-step redox activity similar to the δ-

$Li_xV_2O_5 \cdot nH_2O$ electrode reported previously [31], as the reversible redox peaks corresponding to Li^+ ion intercalation/extraction appear at 2.4V/2.6 V and 2.7 V/2.9 V (**Figure 7a, d**). As the Org:V_2O_5 ratio increased to 1:5, the redox pair at 2.7/2.9 V is diminishing in intensity (**Figure 7b, e**) while the pair at 2.4/2.6V stays at a similar intensity. Additionally, the CV curve of the CTAVO5 electrode shows redox activity at potentials in the range of 3.0 – 3.5 V, indicating that the lithiation/de-lithiation processes involve multiple redox steps. This phenomenon could be ascribed to the multiple Li^+ ion intercalation sites enabled by the pillaring effect of the CTA^+ cations and the resulting relatively large interlayer distance of ~22 Å. When the Org:V_2O_5 ratio increased to 1:2, the CV curve of the DTAVO2 electrode (**Figure 7c**) showed similar electrochemical redox features as observed in the CV curve of the DTAVO5 electrode (**Figure 7b**), however with the peak intensities fading and peaks broadening rapidly over cycling with significant loss of redox activity after five cycles (**Figure 7c**). The redox features shown in the CV curve of the CTAVO2 electrode (**Figure 7f**) are substantially different from other hybrid BVOs and the integral area under the CV curve has substantially narrowed. The rapid peak broadening and fading in the CV curves of both DTAVO2 and CTAVO2 electrodes (**Figure 7c, f**) could be ascribed to the high concentration of the confined linear organic cations in the interlayer region which could lead to the structural instability. Additionally, the large amount of DTA^+/CTA^+ cations could densely pack within the interlayer region of DTAVO2 and CTAVO2, occupying space and creating barriers for the diffusion of electrochemically cycled Li^+ ions thus impairing the electrochemical storage properties of the electrode material.

Figure 8 shows the 1st, 2nd, and 5th cycles of galvanostatic discharge-charge curves acquired in the Li-ion cells containing selected $(DTA)_xV_2O_5$ and $(CTA)_xV_2O_5$ electrodes within a voltage window of 2.0-4.0 V at 20 mA g^{-1}. The potentials of the plateaus in the discharge/charge curves agree with the peaks' potentials shown in the corresponding CV curves, confirming the redox processes of the investigated hybrid phases. The DTAVO20 and CTAVO20 (**Figure 8a, d**) delivered 217.7 mAh g^{-1} and 274.5 mAh g^{-1} in the first discharge cycle, respectively. However, both 1:20 ratio hybrid phases exhibited noticeable first-to-second cycle capacity loss, and the 2nd cycle discharge capacity of DTAVO20 and CTAVO20 dropped and stabilized at around 178 mAh g^{-1} and 245 mAh g^{-1}, respectively. The initial specific capacities of the $(DTA)_xV_2O_5$ and $(CTA)_xV_2O_5$ decrease as the synthesis Org:V_2O_5 molar ratio increases, which could be attributed to the preintercalation of electrochemically inactive DTA^+ and CTA^+ cations. To elaborate, in the first discharge cycle, the DTAVO5 and CTAVO5 electrodes delivered 169.7 mAh g^{-1} and 190 mAh g^{-1}; DTAVO2 and CTAVO2 electrodes delivered 159.3 mAh g^{-1} and 143.0 mAh g^{-1}, respectively. The capacity of DTAVO5 and CTAVO5 electrodes ranges between 169.7-191.7 mAh g^{-1} and 190-210 mAh g^{-1} within the first five cycles, respectively (**Figure 8b, e**). The capacities of the DTAVO2 and CTAVO2 electrodes dropped to 135.2 mAh $g^{-1}$and 121.1 mAh g^{-1} after the 5th cycle, respectively (**Figure 8c, f**). In general, the specific capacity of hybrid BVO electrodes decreased as more DTA^+ or CTA^+ cations were trapped in the

interlayer region, suggesting the high concentration of the confined DTA^+ or CTA^+ cations might densely pack in the interlayer region and may block the intercalation sites and inhibit the transport of Li^+ ions.

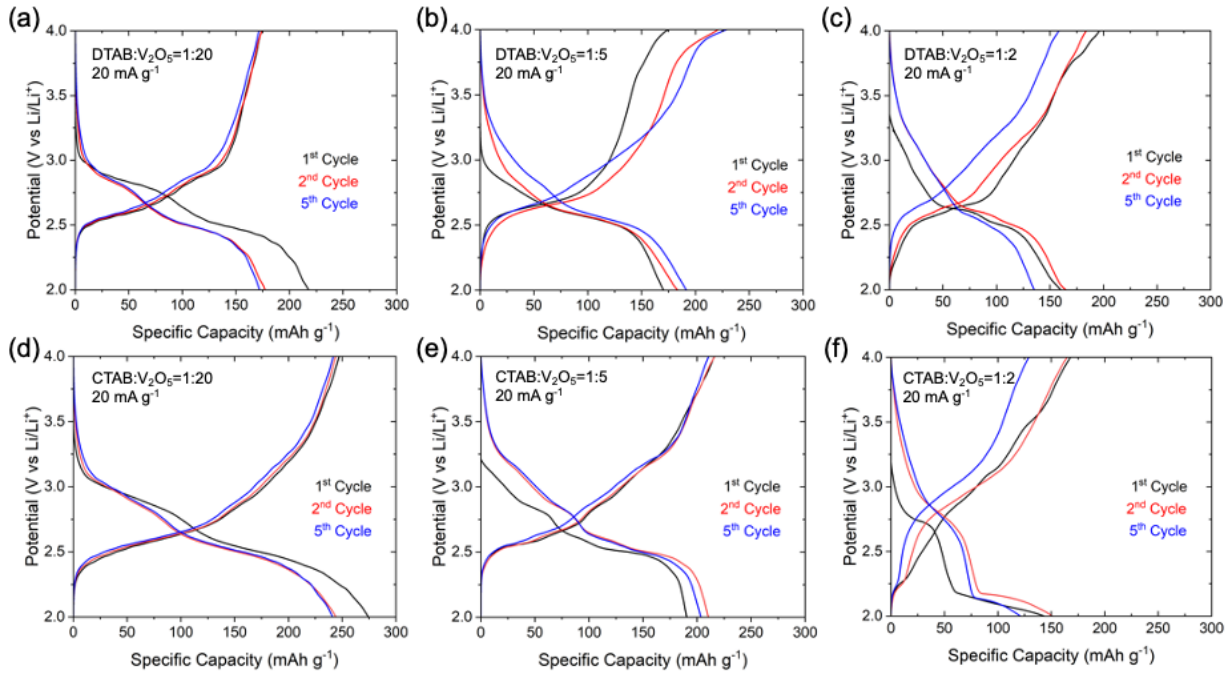

Figure 8. Galvanostatic charge/discharge curves of 1st, 2nd, and 5th cycle of (a-c) $(DTA)_xV_2O_5$ and (d-f) $(CTA)_xV_2O_5$ synthesized using the Org:V_2O_5 molar ratio of (a, d) 1:20, (b, e) 1:5 and (c, f) 1:2 in lithium-ion cells at a current density of 20 mA g^{-1}.

The cycling stability and capacity retention of $(DTA)_xV_2O_5$ and $(CTA)_xV_2O_5$ synthesized using Org:V_2O_5 molar ratio of 1:20, 1:5, and 1:2 in the lithium-ion cells at a current density of 20 mAh g^{-1} are shown in **Figure 9**. After the 50th cycle, the DTAVO20 and CTAVO20 electrodes demonstrated discharge specific capacity of 158.6 mAh g^{-1} and 214.3 mAh g^{-1} with capacity retention of 71.1% and 79.5%, respectively. The DTAVO5 and CTAVO5 electrodes exhibited discharge specific capacity of 95.4 mAh g^{-1} and 154.0 mAh g^{-1} with capacity retention of 49.2% and 73.2% after 50 cycles, respectively. The DTAVO2 and CTAVO2 electrodes demonstrated 68.4 mAh g^{-1} and 62.3 mAh g^{-1} discharge specific capacity with capacity retention of 41.5% and 41.3%, respectively. Interestingly, the specific capacities of DTAVO20 electrode are lower than those shown by the DTAVO5 electrode between 2-10 cycles, but the former outperforms the latter after 10 cycles thus demonstrating a superior extended cycling stability. This trend could be ascribed to the more expanded interlayer region of DTAVO5 phase which could have provided the Li^+ ions with a better diffusivity initially but may have caused the exfoliation of the V-O layers. Similarly, the rapid capacity fading was also shown by the cells containing DTAVO2 and CTAVO2 electrodes. Comparing the cycling stability of the hybrid electrodes synthesized using the same type of linear organic cations but with

different concentrations suggests that a higher concentration of linear organic cations, and consequently larger interlayer distance, would lead to rapid capacity fading, which could be attributed to the active material dissolution in organic electrolyte and/or exfoliation of the V-O layers with the loss of mechanical contact due to a better electrolyte penetration into significantly expanded interlayer regions. AAS characterization of the supernatant solutions obtained after keeping $(DTA)_xV_2O_5$ and $(CTA)_xV_2O_5$ powders in the electrolyte solvent for two days revealed that vanadium concentration increased with the increase of interlayer distances caused by a larger fraction of linear organic cations used in the synthesis (**Figure S6** in **Supporting Information**). The obtained result supports our conclusion that further separating the V-O layers facilitates the active material dissolution in the electrolyte, leading to rapid capacity decay over extended cycling. This observation suggests the cycling stability of hybrid BVOs correlates not only with the interlayer distance but also with the chemical composition of the interlayer region that provides intercalation sites and diffusion pathways for the electrochemically cycled ions.

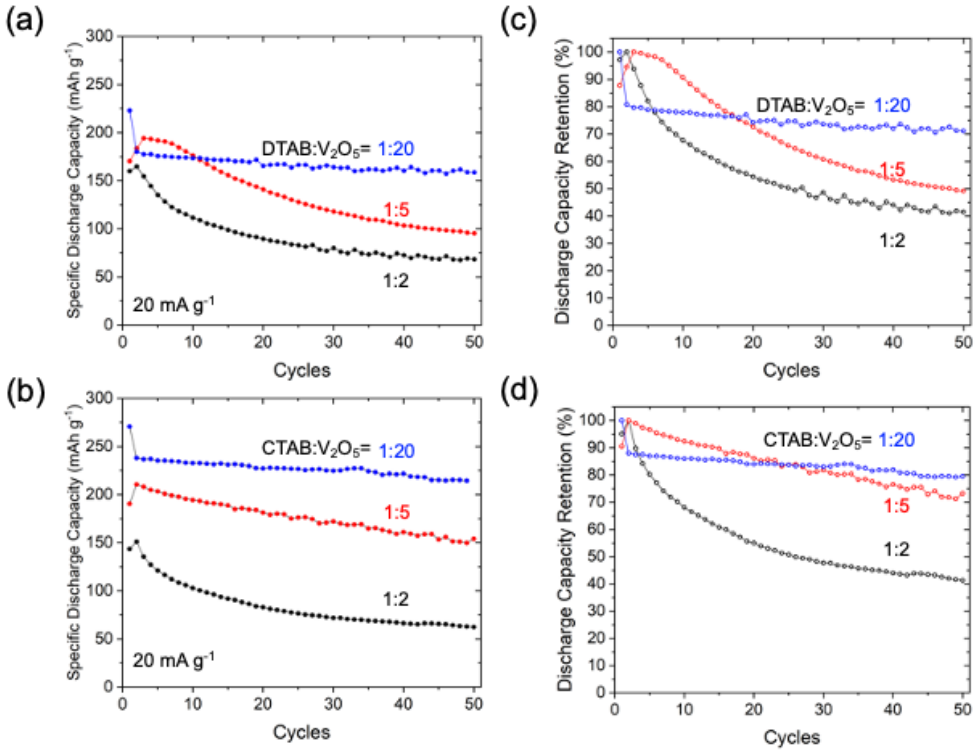

Figure 9. (a, b) Cycling stability and (c, d) capacity retention of the lithium-ion cells containing (a, c) $(DTA)_xV_2O_5$ and (b, d) $(CTA)_xV_2O_5$ electrodes synthesized using Org:V_2O_5 molar ratio of 1:20, 1:5, and 1:2 at a current density of 20 mA g^{-1} over 50 cycles. The capacity retention rates were calculated versus the maximum specific capacity over 50 cycles.

The rate capabilities of the $(DTA)_xV_2O_5$ and $(CTA)_xV_2O_5$ electrodes synthesized with the Org:V_2O_5 molar ratio of 1:20, 1:5, and 1:2 (**Figure 10**) were tested in lithium-ion cells at the step-increased current densities

ranging from 20 mA g^{-1} to 200 mA g^{-1} for 10 cycles each. To evaluate the stability and the recoverability of the hybrid electrodes after cycled at high current densities, the current density was brought back to 20 mA g^{-1} and cycled for another 10 cycles. The summary of the average capacity values at each current density together with the capacity retention data are shown in **Table S1 (Supporting Information)**. The larger capacity drops caused by the current density increase in case of the DTAVO2 and CTAVO2 electrodes could indicate a poorer transport of both ions and electrons due to the blocked diffusion ion pathways by the insulating chemically preintercalated organic cations. The specific capacity values observed at the current density of 20 mA g^{-1} after cycling at the highest current density in this experiment (200 mA g^{-1}) suggest that the hybrid BVOs can tolerate cycling at high current density without significant degradation. Similarly to the cycle life tests, such electrochemical behavior in the rate capability experiment is likely to be caused by dissolution of the $(DTA)_xV_2O_5$ and $(CTA)_xV_2O_5$ electrodes in the electrolytes or exfoliation of the layers leading to the loss of the contact with the electrode which are possible due to the expanded interlayer regions favoring more vigorous interactions with the electrolytes molecules.

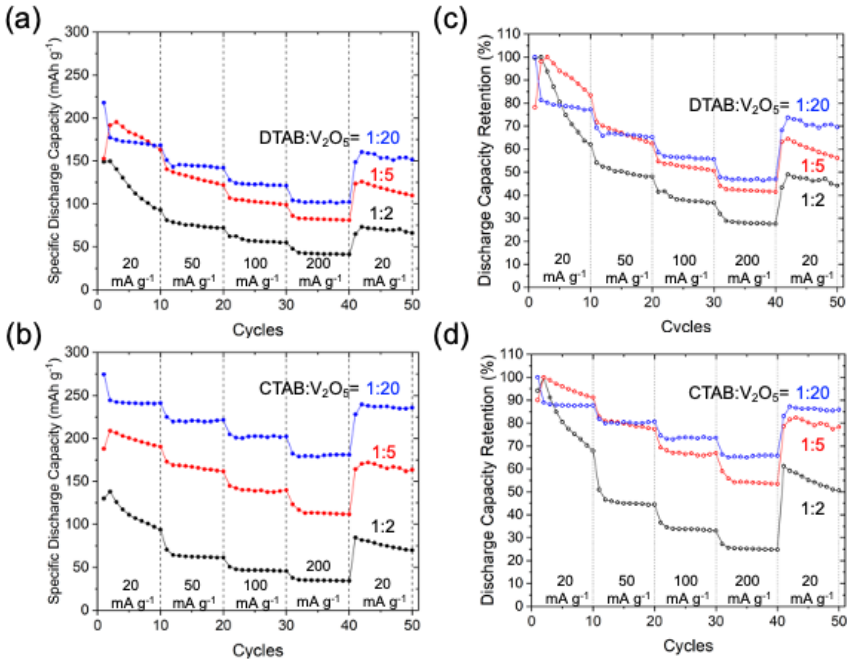

Figure 10. (a, b) Rate capability and (c, d) capacity retention of the lithium-ion cells containing (a, c) $(DTA)_xV_2O_5$ and (b, d) $(CTA)_xV_2O_5$ electrodes synthesized using Org:V_2O_5 molar ratio of 1:20, 1:5, and 1:2 at current density of 20, 50, 100, 200, 20 mA g^{-1} for 10 cycles, respectively. The capacity retention rates were calculated versus the maximum specific capacity.

Conclusions

In summary, we demonstrated that the interlayer distance of hybrid bilayered vanadium oxides (BVOs) can be tuned from 11.1 Å to 35.6 Å by varying the concentration of decyltrimethylammonium (DTA^+) or cetyltrimethylammonium (CTA^+) linear organic cations during chemical preintercalation synthesis. We established a relationship between the interlayer distance, modulated by the concentration of these linear organic cations, and charge storage properties of the resultant hybrid BVOs. Electrochemical behavior of the hybrid BVOs in lithium-ion cells confirmed our hypothesis that the high concentrations of confined DTA^+ or CTA^+ cations result in dense packing within the interlayer regions, obstructing the ion transport pathways for Li^+ ions. Moreover, we observed that increased layer separation enhanced the dissolution of hybrid BVOs in the electrolyte, leading to rapid capacity decay during cycle life and rate capability tests. Our findings report interlayer distances that are unprecedentedly larger than those achieved in previously reported phases preintercalated with inorganic metal ions[19, 30, 31] and most layered materials with the preintercalated organic species[42-45]. The CTAVO20 phase delivered a high initial specific capacity of 274 mAh g^{-1} at 20 mA g^{-1}, maintaining ~180 mAh g^{-1} when cycled at 200 mA g^{-1} in lithium-ion cells. This work paves the way for the chemical preintercalation of redox active organic cations, which can enhance the charge storage capacity of BVOs by introducing new sites for Li^+ ion intercalation within the interlayer region. These insights broaden the functional applicability of hybrid electrode materials, offering significant potential for advancements in energy storage technologies.

Acknowledgements

This work was supported by the National Science Foundation grant DMR-2106445. XRD, SEM and XPS analyses were performed using instruments in the Materials Characterization Core at Drexel University. The scanning transmission electron microscopy portion of this research was supported by the Center for Nanophase Materials Sciences (CNMS), which is a US Department of Energy, Office of Science User Facility at Oak Ridge National Laboratory. We thank Prof. Kevin Owens from the Department of Chemistry at Drexel University for providing us with access to the atomic absorption spectroscopy analysis in the Instrumental Analytical Laboratory.

Author Contributions

X.Z. and E.P. conceived the research and designed the experiments. X.Z. performed the materials synthesis, XRD, SEM, TGA, FTIR, and electrochemical characterizations. R.A. acquired the XPS spectra. T.A. assisted in the analysis and interpretation of the FTIR results. M.J.Z. performed the STEM characterization. All authors participated in the discussion of experimental results and writing this manuscript.

References

(1) Li, W.; Huang, J.; Cao, L.; Liu, Y.; Pan, L.; Feng, L. In Situ Topology Synthesis of Orthorhombic NaV_2O_5 with High Pseudocapacitive Contribution for Lithium-Ion Battery Anode. *ACS Sustainable Chemistry & Engineering* **2019**, *7* (1), 94-99. DOI: 10.1021/acssuschemeng.8b02403.

(2) Hu, M.; Liu, Z.; Zhang, H.; Huang, Z.-H.; Kang, F.; Lv, R. Defect engineering of vanadium pentoxide for efficient lithium-ion storage. *Electrochimica Acta* **2020**, *333*, 135513. DOI: https://doi.org/10.1016/j.electacta.2019.135513.

(3) Zhang, X.; Sun, X.; Li, X.; Hu, X.; Cai, S.; Zheng, C. Recent progress in rate and cycling performance modifications of vanadium oxides cathode for lithium-ion batteries. *Journal of Energy Chemistry* **2021**, *59*, 343-363. DOI: https://doi.org/10.1016/j.jechem.2020.11.022.

(4) He, W.; Xie, Q.-S.; Lin, J.; Qu, B.-H.; Wang, L.-S.; Peng, D.-L. Mechanisms and applications of layer/spinel phase transition in Li- and Mn-rich cathodes for lithium-ion batteries. *Rare Metals* **2022**, *41* (5), 1456-1476. DOI: 10.1007/s12598-021-01896-w.

(5) Huang, Y.; Dong, Y.; Li, S.; Lee, J.; Wang, C.; Zhu, Z.; Xue, W.; Li, Y.; Li, J. Lithium Manganese Spinel Cathodes for Lithium-Ion Batteries. *Advanced Energy Materials* **2021**, *11* (2), 2000997. DOI: https://doi.org/10.1002/aenm.202000997.

(6) Ji, X.; Xia, Q.; Xu, Y.; Feng, H.; Wang, P.; Tan, Q. A review on progress of lithium-rich manganese-based cathodes for lithium ion batteries. *Journal of Power Sources* **2021**, *487*, 229362. DOI: https://doi.org/10.1016/j.jpowsour.2020.229362.

(7) Liu, S.; Wang, B.; Zhang, X.; Zhao, S.; Zhang, Z.; Yu, H. Reviving the lithium-manganese-based layered oxide cathodes for lithium-ion batteries. *Matter* **2021**, *4* (5), 1511-1527. DOI: 10.1016/j.matt.2021.02.023 (acccessed 2024/05/27).

(8) Chakraborty, A.; Kunnikuruvan, S.; Kumar, S.; Markovsky, B.; Aurbach, D.; Dixit, M.; Major, D. T. Layered Cathode Materials for Lithium-Ion Batteries: Review of Computational Studies on $LiNi_{1-x-y}Co_xMn_yO_2$ and $LiNi_{1-x-y}Co_xAl_yO_2$. *Chemistry of Materials* **2020**, *32* (3), 915-952. DOI: 10.1021/acs.chemmater.9b04066.

(9) Tian, C.; Lin, F.; Doeff, M. M. Electrochemical Characteristics of Layered Transition Metal Oxide Cathode Materials for Lithium Ion Batteries: Surface, Bulk Behavior, and Thermal Properties. *Accounts of Chemical Research* **2018**, *51* (1), 89-96. DOI: 10.1021/acs.accounts.7b00520.

(10) Akhilash, M.; Salini, P. S.; John, B.; Mercy, T. D. A journey through layered cathode materials for lithium ion cells – From lithium cobalt oxide to lithium-rich transition metal oxides. *Journal of Alloys and Compounds* **2021**, *869*, 159239. DOI: https://doi.org/10.1016/j.jallcom.2021.159239.

(11) Sun, Y.; Sun, Y.; Wang, R.; Liu, K. Probing the interlayer mechanical coupling of 2D layered materials - A review. *Progress in Natural Science: Materials International* **2022**, *32* (5), 528-537. DOI: https://doi.org/10.1016/j.pnsc.2022.09.008.

(12) Manthiram, A. A reflection on lithium-ion battery cathode chemistry. *Nature Communications* **2020**, *11* (1), 1550. DOI: 10.1038/s41467-020-15355-0.

(13) Boyd, S.; Ganeshan, K.; Tsai, W.-Y.; Wu, T.; Saeed, S.; Jiang, D.-e.; Balke, N.; van Duin, A. C. T.; Augustyn, V. Effects of interlayer confinement and hydration on capacitive charge storage in birnessite. *Nature Materials* **2021**, *20* (12), 1689-1694. DOI: 10.1038/s41563-021-01066-4.

(14) Charles, D. S.; Feygenson, M.; Page, K.; Neuefeind, J.; Xu, W.; Teng, X. Structural water engaged disordered vanadium oxide nanosheets for high capacity aqueous potassium-ion storage. *Nature Communications* **2017**, *8* (1), 15520. DOI: 10.1038/ncomms15520.

(15) Mitchell, J. B.; Lo, W. C.; Genc, A.; LeBeau, J.; Augustyn, V. Transition from Battery to Pseudocapacitor Behavior via Structural Water in Tungsten Oxide. *Chemistry of Materials* **2017**, *29* (9), 3928-3937. DOI: 10.1021/acs.chemmater.6b05485.

(16) Kundu, D.; Adams, B. D.; Duffort, V.; Vajargah, S. H.; Nazar, L. F. A high-capacity and long-life aqueous rechargeable zinc battery using a metal oxide intercalation cathode. *Nature Energy* **2016**, *1* (10), 16119. DOI: 10.1038/nenergy.2016.119.

(17) Fleischmann, S.; Zhang, Y.; Wang, X.; Cummings, P. T.; Wu, J.; Simon, P.; Gogotsi, Y.; Presser, V.; Augustyn, V. Continuous transition from double-layer to Faradaic charge storage in confined electrolytes. *Nature Energy* **2022**, *7* (3), 222-228. DOI: 10.1038/s41560-022-00993-z.

(18) Pomerantseva, E.; Gogotsi, Y. Two-dimensional heterostructures for energy storage. *Nature Energy* **2017**, *2* (7). DOI: 10.1038/nenergy.2017.89.

(19) Zhao, Y.; Han, C.; Yang, J.; Su, J.; Xu, X.; Li, S.; Xu, L.; Fang, R.; Jiang, H.; Zou, X.; et al. Stable Alkali Metal Ion Intercalation Compounds as Optimized Metal Oxide Nanowire Cathodes for Lithium Batteries. *Nano Letters* **2015**, *15* (3), 2180-2185. DOI: 10.1021/acs.nanolett.5b00284.

(20) Choi, J.; Moon, H.; Fleischmann, S. Simultaneous control of crystallite size and interlayer spacing of MoS2 to achieve pseudocapacitive lithium intercalation. *Electrochimica Acta* **2024**, *476*, 143774. DOI: https://doi.org/10.1016/j.electacta.2024.143774.

(21) Tepavcevic, S.; Xiong, H.; Stamenkovic, V. R.; Zuo, X.; Balasubramanian, M.; Prakapenka, V. B.; Johnson, C. S.; Rajh, T. Nanostructured Bilayered Vanadium Oxide Electrodes for Rechargeable Sodium-Ion Batteries. *ACS Nano* **2012**, *6* (1), 530-538. DOI: 10.1021/nn203869a.

(22) Clites, M.; W. Byles, B.; Pomerantseva, E. Bilayered vanadium oxide as the host material for reversible beyond lithium ion intercalation. *Advanced Materials Letters* **2017**, *8* (6), 679-688. DOI: 10.5185/amlett.2017.1536.

(23) Clites, M.; Hart, J. L.; Taheri, M. L.; Pomerantseva, E. Chemically Preintercalated Bilayered $K_xV_2O_5{\cdot}nH_2O$ Nanobelts as a High-Performing Cathode Material for K-Ion Batteries. *ACS Energy Letters* **2018**, *3* (3), 562-567. DOI: 10.1021/acsenergylett.7b01278.

(24) Petkov, V.; Trikalitis, P. N.; Bozin, E. S.; Billinge, S. J. L.; Vogt, T.; Kanatzidis, M. G. Structure of $V_2O_5{\cdot}nH_2O$ Xerogel Solved by the Atomic Pair Distribution Function Technique. *Journal of the American Chemical Society* **2002**, *124* (34), 10157-10162. DOI: 10.1021/ja026143y.

(25) Sun, H.; Zhao, K. Electronic Structure and Comparative Properties of $LiNi_xMn_yCo_zO_2$ Cathode Materials. *The Journal of Physical Chemistry C* **2017**, *121* (11), 6002-6010. DOI: 10.1021/acs.jpcc.7b00810.

(26) Liu, W.; Qin, M.; Gao, C.; Yu, D.; Yue, Y. Green and low-cost synthesis of $LiNi_{0.8}Co_{0.15}Al_{0.05}O_2$ cathode material for Li-ion batteries. *Materials Letters* **2019**, *246*, 153-156. DOI: https://doi.org/10.1016/j.matlet.2019.03.064.

(27) Moretti, A.; Passerini, S. Bilayered Nanostructured $V_2O_5{\cdot}nH_2O$ for Metal Batteries. *Advanced Energy Materials* **2016**, *6* (23), 1600868. DOI: https://doi.org/10.1002/aenm.201600868.

(28) Pomerantseva, E. Chemical Preintercalation Synthesis of Versatile Electrode Materials for Electrochemical Energy Storage. *Accounts of Chemical Research* **2022**. DOI: 10.1021/acs.accounts.2c00193.

(29) Clites, M.; Byles, B. W.; Pomerantseva, E. Effect of aging and hydrothermal treatment on electrochemical performance of chemically pre-intercalated Na–V–O nanowires for Na-ion batteries. *Journal of Materials Chemistry A* **2016**, *4* (20), 7754-7761, 10.1039/C6TA02917E. DOI: 10.1039/C6TA02917E.

(30) Clites, M.; Pomerantseva, E. Bilayered vanadium oxides by chemical pre-intercalation of alkali and alkali-earth ions as battery electrodes. *Energy Storage Materials* **2018**, *11*, 30-37. DOI: 10.1016/j.ensm.2017.09.005.

(31) Ridley, P.; Gallano, C.; Andris, R.; Shuck, C. E.; Gogotsi, Y.; Pomerantseva, E. MXene-Derived Bilayered Vanadium Oxides with Enhanced Stability in Li-Ion Batteries. *ACS Applied Energy Materials* **2020**, *3* (11), 10892-10901. DOI: 10.1021/acsaem.0c01906.

(32) Wan, S.; Musielak, N.; Oliver, A. G.; Jaffe, A. Controlling Electron Delocalization in Vanadium-Based Hybrid Bronzes through Molecular Templation. *Angewandte Chemie International Edition* **2023**, *62* (51), e202314523. DOI: https://doi.org/10.1002/anie.202314523.

(33) Dayaratne, W. L. N.; Torres-Cadena, R.; Schmitt, B. P.; Westrick, E. M.; Jaffe, A. Hybrid bronzes: mixed-valence organic–inorganic metal oxides as a tunable material platform. *Chemical Science* **2023**, *14* (39), 10756-10767, 10.1039/D3SC03828A. DOI: 10.1039/D3SC03828A.

(34) Pomerantseva, E.; Clites, M. Synthesis of hybrid layered electrode materials via chemical pre-intercalation of linear organic molecules. In Low-Dimensional Materials and Devices 2018, 2018.

(35) Holmberg, K. Surfactant-templated nanomaterials synthesis. *Journal of Colloid and Interface Science* **2004**, *274* (2), 355-364. DOI: https://doi.org/10.1016/j.jcis.2004.04.006.

(36) Luca, V.; Hook, J. M. Study of the Structure and Mechanism of Formation through Self-Assembly of Mesostructured Vanadium Oxide. *Chemistry of Materials* **1997**, *9* (12), 2731-2744. DOI: 10.1021/cm960641m.

(37) Chen, X.; Sun, X.; Li, Y. Self-Assembling Vanadium Oxide Nanotubes by Organic Molecular Templates. *Inorganic Chemistry* **2002**, *41* (17), 4524-4530. DOI: 10.1021/ic020092o.

(38) Christensen, C. K.; Bøjesen, E. D.; Sørensen, D. R.; Kristensen, J. H.; Mathiesen, J. K.; Iversen, B. B.; Ravnsbæk, D. B. Structural Evolution during Lithium- and Magnesium-Ion Intercalation in Vanadium Oxide Nanotube Electrodes for Battery Applications. *ACS Applied Nano Materials* **2018**, *1* (9), 5071-5082. DOI: 10.1021/acsanm.8b01183.

(39) Krumeich, F.; Muhr, H. J.; Niederberger, M.; Bieri, F.; Schnyder, B.; Nesper, R. Morphology and Topochemical Reactions of Novel Vanadium Oxide Nanotubes. *Journal of the American Chemical Society* **1999**, *121* (36), 8324-8331. DOI: 10.1021/ja991085a.

(40) Zhou, X.; Wu, G.; Gao, G.; Wang, J.; Yang, H.; Wu, J.; Shen, J.; Zhou, B.; Zhang, Z. Electrochemical Performance Improvement of Vanadium Oxide Nanotubes as Cathode Materials for Lithium Ion Batteries through Ferric Ion Exchange Technique. *The Journal of Physical Chemistry C* **2012**, *116* (41), 21685-21692. DOI: 10.1021/jp306098q.

(41) Ghidiu, M.; Kota, S.; Halim, J.; Sherwood, A. W.; Nedfors, N.; Rosen, J.; Mochalin, V. N.; Barsoum, M. W. Alkylammonium Cation Intercalation into Ti_3C_2 (MXene): Effects on Properties and Ion-Exchange

Capacity Estimation. *Chemistry of Materials* **2017**, *29* (3), 1099-1106. DOI: 10.1021/acs.chemmater.6b04234.

(42) Gong, Y.; Zhou, Y.; Peng, S.; Chen, S.; Fan, S.; Zhang, Q.; He, C.; Jiang, X.; Ren, X. Ferrocene Preintercalated Vanadium Oxides with Rich Oxygen Vacancies for Ultrahigh Rate and Durable Zn-Ion Storage. *Electrochimica Acta* **2023**, *439*, 141693. DOI: https://doi.org/10.1016/j.electacta.2022.141693.

(43) Tong, Y.; Zang, Y.; Su, S.; Zhang, Y.; Fang, J.; Yang, Y.; Li, X.; Wu, X.; Chen, F.; Hou, J.; et al. Methylene blue intercalated vanadium oxide with synergistic energy storage mechanism for highly efficient aqueous zinc ion batteries. *Journal of Energy Chemistry* **2023**, *77*, 269-279. DOI: https://doi.org/10.1016/j.jechem.2022.10.040.

(44) Guo, Y.; Liu, Y.; Li, K.; Gong, Y. Naphthoquinone-intercalated vanadium oxide for high-performance zinc-ion battery. *Journal of Solid State Electrochemistry* **2023**, *27* (10), 2579-2592. DOI: 10.1007/s10008-023-05542-6.

(45) Liu, C. L.; Cao, T.; Wang, Z. P.; Li, K.; Gong, Y.; Zhang, D. L. Redox-active benzoquinone-intercalated layered vanadate for high performance zinc-ion battery: Phenol-keto conversion and the anchoring effect of V-O-V host framework. *Electrochimica Acta* **2022**, *436*, 141447. DOI: https://doi.org/10.1016/j.electacta.2022.141447.

(46) Clites, M.; Andris, R.; Cullen, D. A.; More, K. L.; Pomerantseva, E. Improving Electronic Conductivity of Layered Oxides through the Formation of Two-Dimensional Heterointerface for Intercalation Batteries. *ACS Applied Energy Materials* **2020**, *3* (4), 3835-3844. DOI: 10.1021/acsaem.0c00274.

(47) Zhang, R.; Averianov, T.; Andris, R.; Zachman, M. J.; Pomerantseva, E. Liquid Phase Exfoliation of Chemically Prelithiated Bilayered Vanadium Oxide in Aqueous Media for Li-Ion Batteries. *The Journal of Physical Chemistry C* **2023**. DOI: 10.1021/acs.jpcc.2c06875.

(48) Wang, Y.; Shang, H.; Chou, T.; Cao, G. Effects of Thermal Annealing on the Li^+ Intercalation Properties of $V_2O_5 \cdot nH_2O$ Xerogel Films. *The Journal of Physical Chemistry B* **2005**, *109* (22), 11361-11366. DOI: 10.1021/jp051275+.

(49) Clites, M.; Hart, J. L.; Taheri, M. L.; Pomerantseva, E. Annealing-Assisted Enhancement of Electrochemical Stability of Na-Preintercalated Bilayered Vanadium Oxide Electrodes in Na-Ion Batteries. *ACS Applied Energy Materials* **2020**, *3* (1), 1063-1075. DOI: 10.1021/acsaem.9b02098.

(50) Sanchez, C.; Livage, J.; Lucazeau, G. Infrared and Raman study of amorphous V_2O_5. *Journal of Raman Spectroscopy* **1982**, *12* (1), 68-72. DOI: https://doi.org/10.1002/jrs.1250120110.

(51) Shettigar, R. R.; Misra, N. M.; Patel, K. Cationic surfactant (CTAB) a multipurpose additive in polymer-based drilling fluids. *Journal of Petroleum Exploration and Production Technology* **2018**, *8* (2), 597-606. DOI: 10.1007/s13202-017-0357-8.